A Meshfree Approach for Simulating Fluid Flow in Fractured Porous Media

Anthony R. Lamb [a,Ψ], and Deborah Villarroel-Lamb[b]

[a]AID Consulting Limited, Trinidad and Tobago, West Indies; Email: a.lamb@aidconltd.com
[b]Department of Civil & Environmental Engineering, The University of the West Indies; St. Augustine Campus, Trinidad and Tobago, West Indies; Email: deborah.villarroel-lamb@sta.uwi.edu

[Ψ] *Corresponding Author*

Abstract: *This paper presents a meshfree approach for simulating fluid flow in fractured porous media using a novel fracture (FM) mapping approach. Fracture mapping is a continuum-based approach which simulates the flow interaction between the porous matrix and existing fractures via a transfer function. The approach simulates fluid flow through both the matrix and the fractures and is well suited to models containing sparsely spaced, unconnected fractures. The presented approach determines the fluid flow using approximating functions constructed employing the radial point interpolation method (RPIM) meshfree formulation which uses radial basis functions (RBFs) augmented with polynomials. As part of this meshfree scheme a nodal integration procedure has been implemented thereby removing the need for background integration cells that are usually required for meshfree schemes that rely on Gaussian integration. Numerical test results illustrate the methods ability to adequately describe the fluid pressure fields within a fractured porous domain.*

Keywords: *Fracture Mapping; Fractured porous media; Continuum model; Meshfree method; Radial Point Interpolation; Nodal integration*

1. Introduction

A porous medium can be described as a matrix of solid material with interconnected pores, with at least several continuous paths (Bear, 1988). These pores are void-spaces within the medium that may contain and conduct fluid. When fractures are also present, the medium then consists of two distinct pore spaces which are represented by the void-spaces between fracture walls and the pore spaces within the intact matrix blocks. Conceptual methods developed to quantitatively estimate the flow behaviour in fractured porous media fall into two main categories, continuum methods and discrete fracture methods. The methods that have dominated this area of research are the dual continuum and discrete fracture model approach.

Barenblatt et al. (1960) introduced the dual continuum (DC) concept by modelling flow through a non-deformable, fractured porous medium. The dual continuum concept provides a mathematical framework for the fluid flow interaction between the matrix domain and fractures and was originally applied to the field of reservoir engineering by Warren and Root (1963) to characterise and simulate fluid flow in naturally fractured reservoirs. The dual continuum concept can be subdivided into the dual porosity and dual permeability approach (Diodato, 1994). The dual porosity approach assumes that the porous matrix is discontinuous and flow within the domain is achieved via the fractured network. The simulated fluid flow is therefore directly affected by fracture network connectivity and distribution. In contrast, the dual permeability model assumes that the matrix is continuous and fluid flow occurs within both the matrix and fractures (Fung, 1991; Diodato, 1994; Zhang and Sanderson, 2002). Fracture network connectivity is not a prerequisite when using the dual permeability method. DC approaches are very simple to implement; however, since these methods rely on averaged properties, they cannot adequately simulate fluid flow in highly heterogeneous domains. Since the approach does not consider fracture geometry and orientation it is unable to accurately determine the influence large scale fractures have on fluid flow within a domain.

The discrete fracture method has received considerable interest over the last few years in the field of reservoir simulation and hydrology (Lee et al., 1999; Kim and Deo, 2000; Karimi-Fard et al., 2004; Matthäi et al., 2007; Tran and Ravoof, 2007; Geiger-Boschung et al., 2009). In this approach, fractures are explicitly discretized along with the matrix domain. Although this method considers real fracture geometry, size and orientation, its demands on computer storage for models containing hundreds or thousands of fractures limits its applicability to domains with low fracture density.

Generating computational meshes incorporating fractures are also challenging and time consuming.

The fracture mapping approach presented combines the merits of both the discrete and continuum approaches; fracture geometry is preserved without having to mesh existing fractures within the simulation domain. In the finite element (FE) implementation, elements intersected by a fracture are treated as two overlapping elements; a matrix element and a fracture element (Lamb, 2011). The orientation and permeability of the fracture are then mapped to the fracture element and the transfer function presented by Barenblatt et al. (1960) is adopted to account for fluid flow interaction between the overlapping matrix and fracture elements. Although this method is able to adequately simulate the fracture geometry the accuracy of the FE implementation solution is dependent on the size of the elements used for the fracture mapping (Lamb, 2011). To remove this mesh dependence a meshfree approach has been proposed and presented in this manuscript.

Meshfree methods evolved from the need to reduce the dependence on a mesh in the formulation of numerical solutions. One of the most attractive features of meshfree methods is that there is less reliance on mesh quality for conducting numerical simulations (Liu, 2010). These methods use a set of nodes scattered within the problem domain as well as along the boundaries of the domain to represent the problem domain and its boundaries. These methods include, among others, the discrete element method (DEM) (Cundall and Strack, 1979), element free Galerkin (EFG) (Belytschko et al., 1994), and the radial point interpolation method (RPIM) (Wang and Liu, 2002).

In the DEM, computational points are associated with a finite size and shape. Interaction between points (particles) occurs only where they are in contact - according to the specified interaction rules. This method is very well suited to modelling fractures since particle interactions can take the form of breakable bonds, however, DEMs are processor intensive and this limits either the length of a simulation or the number of particles.

EFG is a continuum method in which the shape functions are calculated using the moving least-squares method (MLS). Shape functions constructed using MLS do not satisfy the Kronecker delta function properties, i.e., the shape function at the node is equal to one and zero for all other nodes used to construct the shape function. These shape functions therefore have the following disadvantages: 1) difficulties in the implementation of essential boundary conditions, and 2) complexity of algorithms to construct shape functions. Several methods have been proposed to overcome these disadvantages for example the Lagrangian method (Lu et al., 1994), the penalty method (Onate et al., 1996) and the collocation method (Wagner and Liu, 2000) for essential boundary conditions. Analytical integration (Lancaster and Salkauskas, 1981), the recursive method

(Breitkopf et al., 2000) and parallel computing (Danielson et al., 2000) have been proposed for the construction of shape functions.

The RPIM formulation combines radial and polynomial basis functions to address the problems of implementing essential boundary conditions and construction of shape functions (2002). Inclusion of radial basis functions overcome possible singularity associated with meshfree methods based on only the polynomial basis (Liu and Gu, 2001). The interpolation (shape) function obtained passes through all scattered points in an influence domain and thus satisfy the Kronecker delta function property. This makes the implementation of essential boundary conditions much easier than meshfree methods based on the moving least-squares approximation, e.g., the element free Galerkin method.

The finite element method relies on the use of Gaussian integration over elements to solve the discretized system equations. Meshfree methods also employ Gaussian integration; however, since these methods do not rely on an element framework, a background mesh independent of the nodal arrangement, is required for numerical integration. The aim of nodal integration schemes is to eliminate the need for a background mesh for numerical integration (Beissel and Belytschko, 1996; Chen et al., 2001). Since direct nodal integration usually results in instabilities in the numerical solution Taylor series expansion terms have been added to the numerical integration of the RPIM formulation by Liu et al. (2007). NI-RPIM has been used in this study for the implementation of the meshfree fracture mapping approach.

The remainder of this document is outlined as follows. The governing equations which describe fluid flow in porous media are firstly presented followed by a description of the proposed fracture mapping approach used to capture the flow interaction between the porous matrix and fracture in the meshfree domain. The RPIM shape functions and the nodal integration procedure are then presented along with the governing equations and their discretized form. A brief outline of the meshfree implementation procedure is also presented.

Finally, the meshfree approach is validated using the closed-form solution for fluid flow in a rectangular reservoir intersected by a vertical fracture. The second numerical test included provides a comparison of the proposed numerical approach with the conventional discrete fracture model approach.

2. Governing Equations

This section presents the equations which describe single phase fluid flow through porous media. This single-phase fluid flow through porous media can be described by Darcy's law:

$$\boldsymbol{v}_d = \frac{\mathbf{K}}{\mu}\left(-\nabla P_w + \rho \mathbf{g}\right), \tag{1}$$

where v_d is Darcy's velocity, **K**, is the spatially varying permeability tensor of the porous medium concerned, μ is the fluid viscosity, P_w is the pore fluid pressure, **g** is gravity and ρ is fluid density.

Continuity or mass conservation is a second important law in the development of the flow equations; for continuity the amount of fluid flowing into a control volume is equal to the amount flowing out. Therefore, the continuity equation is given by:

$$\nabla \cdot \boldsymbol{v}_d = Q_w, \tag{2}$$

where Q_w is the specified source/sink term. Combining (1) and (2) results in the single phase, elliptical pressure equation:

$$\nabla \cdot \left(\frac{\mathbf{K}}{\mu} \left(-\nabla P_w + \rho \mathbf{g} \right) \right) = Q_w, \tag{3}$$

The steady state flow equations for both the matrix and fractures then take the forms:
For the matrix:

$$\nabla \cdot \left(\frac{\mathbf{K}_m}{\mu} \left(-\nabla P_{wm} + \rho \mathbf{g} \right) \right) + \frac{\overline{\mathbf{s}} \mathbf{K}_f}{\mu} \left(P_{wm} - P_{wf} \right) = Q_w, \tag{4}$$

and for the fractures:

$$\nabla \cdot \left(\frac{\mathbf{K}_f}{\mu} \left(-\nabla P_{wf} + \rho \mathbf{g} \right) \right) - \frac{\overline{\mathbf{s}} \mathbf{K}_f}{\mu} \left(P_{wm} - P_{wf} \right) = 0, \tag{5}$$

The transient flow equation is obtained by including the specific storage of the medium given by, $n \, / \, K_w$, assuming incompressible grains. The domain porosity is represented by n and K_w represents the bulk modulus of the fluid (see Istok (1989)) for a detailed derivation of the specific storage coefficient).

The transient flow equations take the form:

$$\nabla \cdot \left(\frac{\mathbf{K}_m}{\mu} \left(-\nabla P_{wm} + \rho \mathbf{g} \right) \right) - \frac{\overline{\mathbf{s}} \mathbf{K}_f}{\mu} \left(P_{wm} - P_{wf} \right) + \frac{n_m}{K_w} \frac{\partial P_{wm}}{\partial t} = Q_w, \tag{6}$$

for the porous matrix, and,

$$\nabla \cdot \left(\frac{\mathbf{K}_f}{\mu} \left(-\nabla P_{wf} + \rho \mathbf{g} \right) \right) - \frac{\overline{\mathbf{s}} \mathbf{K}_f}{\mu} \left(P_{wm} - P_{wf} \right) + \frac{n_f}{K_w} \frac{\partial P_{wf}}{\partial t} = 0, \tag{7}$$

The first numerical example presented in this paper solves the transient pressure equation and the second example solves the steady state pressure equation.

3. Fracture Mapping

This section presents the meshfree FM approach that is used to capture the flow interaction between the porous matrix and existing fractures. In this numerical approach both the porous matrix and fracture are discretized using nodes within the computational domain. Fractures that exist within the domain are treated as the superposition of porous matrix and fracture discretization nodes (see Figure 1). The transfer function adopted in this study is based on the quasi steady-state function proposed by Barenblatt et al. (1960), which assumes that the flow within a discretization node is directly proportional to the

difference between the matrix pore pressure and the fracture fluid pressure.

The transfer function T_r, implemented is given by:

$$T_r = \frac{\overline{\mathbf{s}} \mathbf{K}_f}{\mu_w} \left(P_{wm} - P_{wf} \right), \tag{8}$$

where $\mathbf{K}_f$ is the fracture permeability, μ_w is the fluid viscosity, P_{wm} is the matrix fluid pore pressure, P_{wf} is the fracture fluid pressure. The fracture permeability can be determined using the following relationship proposed by Witherspoon et al. (1980):

$$\mathbf{K}_f = \frac{b^2}{12}, \tag{9}$$

where b is the fracture width. In the original transfer function presented by Barenblatt *et al.* (1960), $\overline{\mathbf{S}}$ represents a shape factor which accounts for the fracture size and geometry. Since the FM accounts for the width and geometry of fractures within the domain, the shape factor is not required; however, it has been retained to ensure dimensional consistency when the transfer function is introduced into the equations of fluid flow. The variable $\overline{\mathbf{S}}$ has dimension L^{-2}, where L represents length; $\overline{\mathbf{S}}$ has been assigned a value of 1.

The amount of fluid transferred between the matrix and fracture elements is characterised by the fracture permeability, $\mathbf{K}_f$.
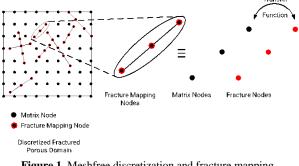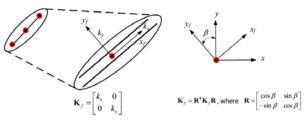

Figure 1. Meshfree discretization and fracture mapping

The nodal permeability is taken as element $\mathbf{K}_{fn} = \mathbf{K}'_f$, which represents the fracture permeability aligned to the global Cartesian axes (see Figure 2).

Figure 2. Fracture permeability alignment with the Cartesian axes using the rotation tensor **R**

This mapping equates the total flow through the fracture nodes to the total flow through porous matrix nodes.

4. RPIM Shape Functions

The radial point interpolation method (RPIM) is formulated based on the Galerkin weak form using shape functions that satisfy the Kronecker delta function property. These shape functions are created through an interpolation using local nodes with both radial and polynomial basis functions. Such an interpolation is often used by many researchers for curve or surface fitting and function approximation (Golberg, 1996). The procedure of constructing RPIM shape functions is as follows.

The function $u(\mathbf{x})$ is approximated using radial and polynomial basis functions in the form of

$$u(\mathbf{x}) = \sum_{i=1}^{n} R_i(\mathbf{x})a_i + \sum_{j=1}^{m} P_j(\mathbf{x})b_j = \mathbf{R}^T(\mathbf{x})\mathbf{a} + \mathbf{P}^T(\mathbf{x})\mathbf{b}, \quad (10)$$

where $R_i(\mathbf{x})$ and $P_j(\mathbf{x})$ are radial polynomial basis functions in two-dimensional space $\mathbf{x}^T = [x,y]$, n is the number of field nodes in the local support domain of point $\mathbf{x}$, m is the number of terms of polynomial basis functions, and a_i and b_j are coefficients for $R_i(\mathbf{x})$ and $P_j(\mathbf{x})$, respectively. These vectors are defined as:

$$\mathbf{R}(\mathbf{x}) = \left[R_1(\mathbf{x}), R_2(\mathbf{x}), R_3(\mathbf{x}),...,R_n(\mathbf{x}) \right]^T,$$
$$\mathbf{P}(\mathbf{x}) = \left[P_1(\mathbf{x}), P_2(\mathbf{x}), P_3(\mathbf{x}),...,P_n(\mathbf{x}) \right]^T,$$
$$\mathbf{a} = \left[a_1, a_2, a_3,...,a_n \right]^T,$$
$$\mathbf{b} = \left[b_1, b_2, b_3,...,b_m \right]^T. \quad (11)$$

The radial basis function $R_i(\mathbf{x})$ has the following general form:

$$R_i(\mathbf{x}) = R(r_i), \quad (12)$$

where r_i is the distance between the interpolating point $\mathbf{x}$ and field node x_i and is expressed as:

$$r_i = \sqrt{(x - x_i)^2 + (y - y_i)^2} \quad \text{for 2-D problems.} \quad (13)$$

The polynomial basis vector $\mathbf{P}(\mathbf{x})$ has the following form for two-dimensional problems:

$$\mathbf{P}(\mathbf{x}) = \left[1, x, y, x^2, xy, y^2,... \right]^T. \quad (14)$$

Linear polynomials are used for the numerical examples presented in this paper. In order to determine a_i and b_j of (10), a support domain is constructed for the point of interest at $\mathbf{x}$, with n field nodes included in the support domain (see Figure 3). The coefficient vectors $\mathbf{a}$ and $\mathbf{b}$ are then determined by ensuring that the displacement of all the n field nodes within the local support domain satisfy (10).

This leads to n linear equations, one for each node and can be expressed in the following matrix form:

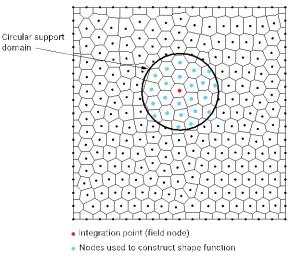$$\mathbf{U}_s = \mathbf{R}_0 \mathbf{a} + \mathbf{P}_m \mathbf{b}, \quad (15)$$

Figure 3. Selection of supporting nodes required for shape function

where $\mathbf{U}_s$ is the vector of approximate function values is given. $\mathbf{R}_o$ and $\mathbf{P}_m$ represent the moment matrix of radial basis functions and polynomial moment matrix respectively. To ensure that the linear equations have a unique solution the following constraint is also added:

$$\sum_{i=1}^{n} P_j(x_i, y_i)a_i = 0 \qquad j = 1,2,...,m. \quad (16)$$

The system equations are now expressed as:

$$\begin{bmatrix} \mathbf{U}_s \\ 0 \end{bmatrix} = \begin{bmatrix} \mathbf{R}_0 & \mathbf{P}_m \\ \mathbf{P}_m^T & 0 \end{bmatrix} \begin{bmatrix} \mathbf{a} \\ \mathbf{b} \end{bmatrix} = \mathbf{G} \begin{bmatrix} \mathbf{a} \\ \mathbf{b} \end{bmatrix}. \quad (17)$$

The function approximation is now expressed as:

$$\mathbf{u}(\mathbf{x}) = \left[\mathbf{R}^T(\mathbf{x}) \mathbf{P}^T(\mathbf{x}) \right] \mathbf{G}^{-1} \begin{bmatrix} \mathbf{U}_s \\ 0 \end{bmatrix} = \mathbf{N}(\mathbf{x})\mathbf{U}_s, \quad (18)$$

where the matrix of shape functions $\mathbf{N}(\mathbf{x})$ is defined by:

$$\mathbf{N}(\mathbf{x}) = \left[N_1(\mathbf{x}), N_2(\mathbf{x}), N_3(\mathbf{x}),...,N_n(\mathbf{x}) \right], \quad (19)$$

where the kth shape function is defined as:

$$N_k(\mathbf{x}) = \sum_{i=1}^{n} B_i(\mathbf{x})\bar{G}_{i,k} + \sum_{j=1}^{m} P_j(\mathbf{x})\bar{G}_{n+j,k}. \quad (20)$$

where $\bar{G}_{i,k}$ is the (i,k) element of $\mathbf{G}^{-1}$.

Using the inverse of matrix $\mathbf{G}$ the shape functions are obtained via:

$$\frac{\partial N_k}{\partial x} = \sum_{i=1}^{n} \frac{\partial B_i}{\partial x} \bar{G}_{i,k} + \sum_{j=1}^{m} \frac{\partial P_j}{\partial x} \bar{G}_{n+j,k}$$
$$\frac{\partial N_k}{\partial y} = \sum_{i=1}^{n} \frac{\partial B_i}{\partial y} \bar{G}_{i,k} + \sum_{j=1}^{m} \frac{\partial P_j}{\partial y} \bar{G}_{n+j,k} \quad (21)$$

The radial basis function used in this work is the multi-quadratics radial basis function (MQ-RBF) given by:

$$R_i(x,y) = \left(r_i^2 + (\alpha_c d_c)^2\right)^q,$$ (22)

where d_c is the characteristic length that relates to the nodal spacing in the support domain of the field node **x** and is usually taken as the average nodal spacing for all the nodes in the support domain, q and α_c are shape parameters. The values used of q and α_c used for the numerical examples presented are 1.03 and 2.5 respectively.

5. Nodal Integration

The integrals of any discrete variable are numerically determined over individual elements and summed for all elements to obtain the global integration. Using the Gaussian quadrature scheme the numerical integration can be written as:

$$\int_\Omega f(x,y)\,d\Omega = \sum_{k}^{ne}\sum_{i=1}^{ng} w_i f\left(x_{ip},y_{ip}\right)\left|J_{ik}\right|$$ (23)

where $f(x,y)$ is the integrand applicable over domain Ω, w_i is the Gauss weighting factor for the i Gauss point at (x_{ip}, y_{ip}) and J_{ik} is the Jacobian matrix for the finite element k. ne and ng are the number of elements and Gaussian integration points respectively.

NI-RPIM uses the Taylor series extension to carry out the integration over Voronoi integration cells (Figure 4). The integral function is extended to include additional terms of the Taylor series, and the integration will be approximately performed on these terms. Therefore, the Taylor series extension of the integrand $f(x,y)$ can be written as a two-dimensional (2D) continuous function $f(x,y)$ can be approximated in the vicinity of a point (x_o, y_o) as follows:

$$f(x,y) \approx f(x_0,y_0) + \left(x\frac{\partial}{\partial x} + y\frac{\partial}{\partial y}\right)f(x_0,y_0) +$$
$$\frac{1}{2!}\left(x\frac{\partial}{\partial x} + y\frac{\partial}{\partial y}\right)^2 f(x_0,y_0)$$ (24)

The integral over the nodal integration domain Ω_i (Voronoi cell i) can be expressed as:

$$\iint_{\Omega_i} f(x,y)\,d\Omega$$
$$\approx \iint_{\Omega_i}\left(f(x_0,y_0) + \left(x\frac{\partial}{\partial x} + y\frac{\partial}{\partial y}\right)f(x_0,y_0) + \frac{1}{2!}\left(x\frac{\partial}{\partial x} + y\frac{\partial}{\partial y}\right)^2 f(x_0,y_0)\right)d\Omega$$
$$= f(x_0,y_0)\iint_{\Omega_i}1\,d\Omega + f_{,x}(x_0,y_0)\iint_{\Omega_i}x\,d\Omega + f_{,y}(x_0,y_0)\iint_{\Omega_i}y\,d\Omega +$$
$$\frac{1}{2}f_{,xx}(x_0,y_0)\iint_{\Omega_i}x^2\,d\Omega + f_{,xy}(x_0,y_0)\iint_{\Omega_i}xy\,d\Omega + \frac{1}{2}f_{,yy}(x_0,y_0)\iint_{\Omega_i}y^2\,d\Omega$$
$$= f(x_0,y_0)A_i + f_{,x}(x_0,y_0)M_{yi} + f_{,y}(x_0,y_0)M_{xi} +$$
$$\frac{1}{2}f_{,xx}(x_0,y_0)M_{yyi} + f_{,xy}(x_0,y_0)M_{xyi} + \frac{1}{2}f_{,yy}(x_0,y_0)M_{xxi}$$ (25)

where A_i is the area of the nodal integration domain of the ith node,

$$M_{xi} = \iint_{A_i} y\,dA_i \qquad M_{yi} = \iint_{A_i} x\,dA_i$$ (26)

are the area moments of the first-order for the integration domain of the ith node, and

$$M_{xxi} = \iint_{A_i} y^2\,dA_i \quad M_{yyi} = \iint_{A_i} x^2\,dA_i \quad M_{xyi} = \iint_{A_i} xy\,dA_i$$ (27)

are the area moments of second-order for the integration domain of the ith node.
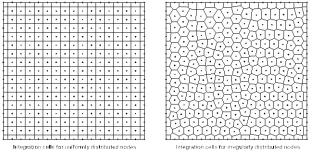

Figure 4. Voronoi cells used for nodal integration

6. Spatial Discretization

Applying the Galerkin approach to the steady state elliptic pressure equation, neglecting the effects of gravity, the resulting discretized equations take the form:

$$\begin{bmatrix} \mathbf{H}_m + \mathbf{H}_{T_r} & -\mathbf{H}_{T_r} \\ -\mathbf{H}_{T_r} & \mathbf{H}_f + \mathbf{H}_{T_r} \end{bmatrix}\begin{bmatrix} \bar{\mathbf{P}}_{wm} \\ \bar{\mathbf{P}}_{wf} \end{bmatrix} = \begin{bmatrix} \mathbf{Q} \\ \mathbf{0} \end{bmatrix},$$ (28)

where,
$\mathbf{H}_m$ is the porous medium permeability matrix,

$$\mathbf{H}_m = \int_\Omega (\nabla \mathbf{N}_p)^T \frac{\mathbf{K}_m}{\mu_w}\nabla\mathbf{N}_p\,d\Omega,$$ (29)

$\mathbf{H}_f$ is the fracture permeability matrix,

$$\mathbf{H}_f = \int_\Omega (\nabla \mathbf{N}_p)^T \frac{\mathbf{K}_f}{\mu_w}\nabla\mathbf{N}_p\,d\Omega,$$ (30)

$\mathbf{H}_{Tr}$ is the transfer matrix,

$$\mathbf{H}_{T_r} = \int_\Omega \mathbf{N}_p^T \frac{\bar{s}\mathbf{K}_f}{\mu_w}\mathbf{N}_p\,d\Omega,$$ (31)

$\mathbf{Q}$ is the flow field vector

$$\mathbf{Q} = \int_\Gamma \mathbf{N}_p^T Q_w\,d\Gamma,$$ (32)

$\bar{\mathbf{P}}_{wm}$ and $\bar{\mathbf{P}}_{wf}$ are vectors representing the nodal pressures for the matrix and fracture, respectively.

7. Implementation

The implementation of the NI-RPIM fracture mapping has the following steps:
1. Domain discretization: nodes are used to describe both the domain and existing fracture. Domain pore pressures are approximated at these node locations;

2. Generate Voronoi cells for nodal integration: Cells are generated using a MATLAB® Executable (MEX) interface to Voro++ (Rycroft et al., 2006);
3. Loop over all nodes:
   a. Determine area of Voronoi Cell along with first and second moment area of the cell corresponding to current node;
   b. Determine shape functions associated with the current node;
   c. Evaluate nodal contributions to the discrete system Equation (28): nodes that describe the fracture contribute to the fracture permeability and transfer matrix ($\mathbf{H}_f$ and $\mathbf{H}_{Tr}$), and
   d. Assemble nodal contribution of current node to form global system matrices.
4. Apply boundary conditions, and
5. Solve system equations to obtain field variable, in this instance nodal pore pressures.

8. Numerical Tests

Numerical experiments are presented to validate the meshfree fracture mapping approach. The first numerical example compares the FEM and meshfree solutions to the analytical solution for a vertical fracture intersecting a well in a closed reservoir. The second example is used to compare the results obtained from the mapping against those obtained from a discrete fracture representation.

One well intersecting a vertical fracture

This example assesses the accuracy of the fracture mapping code by simulating a well fully penetrating a fractured confined reservoir. The model dimensions and properties are shown in Figure 4. The fracture is aligned with the *x*-axis and is located at the centre of a square region of a confined reservoir. It is assumed to intersect a fully penetrating well at the centre of the reservoir. The analytical solution for this problem has been presented by Gringarten et al. (1974). The pressure drop on the fracture is given by:

$$P_w = 2\pi \int_0^{t_{DA}} \left[1 + 2\sum_{k=1}^{\infty} \exp\left(-(2k\pi)^2 t_{DA}\right) \right]$$

$$\left[1 + 2\sum_{k=1}^{\infty} \exp\left(-(2k\pi)^2 t_{DA}\right) \frac{\sin\left(k\pi \frac{x_f}{x_e}\right)}{k\pi \frac{x_f}{x_e}} \cos\left(k\pi \frac{x_f}{x_e}\right) \right] dt_{DA}, \quad (33)$$

where t_{DA} represents the dimensionless time based on the drainage area and is given by:

$$t_{DA} = \frac{Tt}{4S_c (x_e y_e)^2}, \quad (34)$$

where T is the matrix transmissivity, t represents time and S_c is the matrix storage coefficient. x_f and x_e represent the fracture half-length and rectangular reservoir half dimensions respectively (see Figure 5).

Given the symmetry of the domain, only one-quarter of the domain was discretized for the numerical simulations. The discretizations used for the numerical solutions are shown in Figure 6. In the meshfree implementation a refinement is obtained by increasing the number of nodes that describe the fracture. A coarse discretization is used in this example to illustrate the effectiveness of the proposed fracture mapping approach. A comparison of the analytical and proposed meshfree procedure is given in Figure 7.
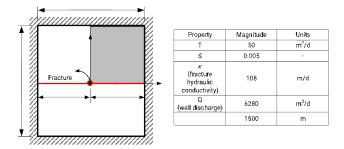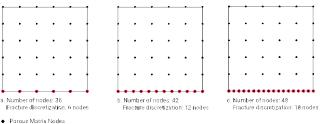
Property	Magnitude	Units
T	50	m²/d
S	0.005	-
κ (fracture hydraulic conductivity)	108	m/d
Q (well discharge)	6280	m³/d
	1500	m

Figure 5. Closed rectangular reservoir containing a well intersected by a vertical fracture

a. Number of nodes: 36
Fracture discretization: 6 nodes

b. Number of nodes: 42
Fracture discretization: 12 nodes

c. Number of nodes: 48
Fracture discretization: 18 nodes

● Porous Matrix Nodes
● Porous Matrix/Fracture Nodes

Figure 6. Domain discretizations used for quarter of the closed rectangular reservoir
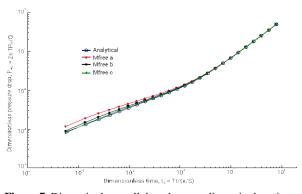
Figure 7. Dimensionless well drawdown vs dimensionless time, showing comparison of numerical and analytical solutions

The computed well drawdown versus dimensionless time for the discretization labeled Mfree *c* is given in Table 1 for both the FEM and meshfree implementation. The numerical results obtained show good agreement with the analytical solution having a variation ranging from 0% to 5.5%. The NI-RPIM therefore provides a good solution approximation.

Table 1. Computed well drawdown vs dimensionless

Time t (days)	Dimensionless Time $t_d = \dfrac{Tt}{x_f^2 S_c}$	Dimensionless Pressure drop $P_{wd} = \dfrac{2\pi T P_w}{Q}$		% Variation between Analytical and Meshfree Solutions
		Analytical	Meshfree	
0.50	5.56E-04	0.0835	0.0811	2.9
1.21	1.34E-03	0.1298	0.1342	3.4
2.21	2.45E-03	0.1755	0.1848	5.3
3.62	4.02E-03	0.2248	0.2372	5.5
5.62	6.24E-03	0.2801	0.2944	5.1
8.45	9.38E-03	0.3434	0.3586	4.4
12.44	1.38E-02	0.4168	0.4325	3.8
18.09	2.01E-02	0.5026	0.5185	3.2
26.08	2.90E-02	0.6035	0.6195	2.7
37.38	4.15E-02	0.7227	0.7392	2.3
53.36	5.93E-02	0.8654	0.8840	2.1
75.95	8.44E-02	1.0424	1.0653	2.2
107.89	0.12	1.2740	1.3022	2.2
153.06	0.17	1.5917	1.6242	2.0
216.92	0.24	2.0380	2.0726	1.7
307.22	0.34	2.6684	2.7038	1.3
434.92	0.48	3.5599	3.5954	1.0
615.47	0.68	4.8204	4.8558	0.7
870.78	0.97	6.6028	6.6375	0.5
1231.78	1.37	9.1230	9.1562	0.4
1742.23	1.94	12.6867	12.7162	0.2
2464.02	2.74	17.7257	17.7472	0.1
3484.62	3.87	24.8508	24.8554	0.0
4927.75	5.48	34.9258	34.8952	0.1
6968.34	7.74	49.1718	49.0691	0.2

9. Discrete Fracture Comparison

In this example, the steady state pressure equation (Equations (4) and (5)) is solved on a fractured domain using the discrete fracture model (DFM) and the proposed meshfree fracture mapping approach. The rates of convergence of each method are determined and the pressure field obtained within the domain is also compared. The model used in this numerical example is shown in Figure 8

Figure 8. 2D fractured domain with applied pressures at top and bottom boundaries

The finite element discrete fracture model in this example uses triangular, three-noded elements (T3) to discretize the matrix and two-noded linear line (L2) elements to discretize the fracture (see Figure 9).

Prior to comparing DFM to the fracture mapping approach, the rate of convergence of DFM was determined. Three of the six meshes used to determine the rate of convergence of DFM are shown in Figure 10. The mesh refinements used to determine the rate of convergence of DFM were obtained by dividing each element of the preceding mesh into four new elements using Mesh A as the base mesh (Figure 10(a)).
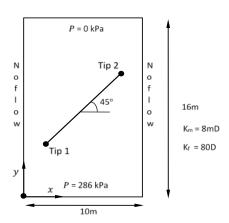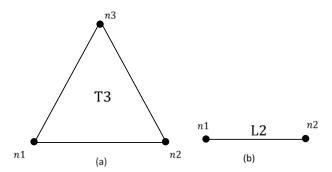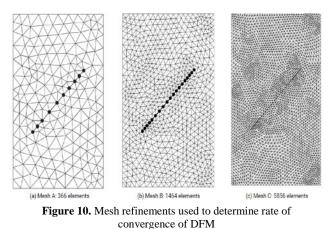

Figure 9. Elements used for discrete fracture model. (a) Triangular element (T3) used to discretize the matrix and (b) line element (L2) used to discretize the fracture

The mesh used as the reference mesh for the convergence study contained 374784 elements (fifth

refinement step); at higher resolutions the discretization is not clearly shown and therefore have not been included. The third (23424 elements) and fourth (93696 elements) refinement steps were also used in determining the rate of convergence.

Figure 10. Mesh refinements used to determine rate of convergence of DFM

The error was measured using the normalised L_2 norm defined by:

$$\frac{\| \mathbf{p}_c - \mathbf{p}_{ref} \|_b}{\| \mathbf{p}_{ref} \|_b} = \frac{\left(\int_{\mathbf{\Omega}} \left(\mathbf{p}_c - \mathbf{p}_{ref} \right)^2 d\mathbf{\Omega} \right)^{\frac{1}{2}}}{\left(\int_{\mathbf{\Omega}} \left(\mathbf{p}_{ref} \right)^2 d\mathbf{\Omega} \right)^{\frac{1}{2}}}, \qquad (35)$$

where $\mathbf{p}_c$ is the pressure determined from a coarse mesh and $\mathbf{p}_{ref}$ is the pressure determined on the reference mesh. The rate of convergence is given by the gradient of the log-log plot of the L_2 error norm vs. the nodal spacing h. The rate of convergence was obtained using linear regression of the data points and is equal to 1.21.

Using the DFM reference solution the rates of convergence of the Meshfree implementation of FM were also determined. The discretizations used to determine the rates of convergence are shown in Figure 11. The number of nodes for the discretizations are 289, 1089, 4225 and 16641 respectively. The convergence rates are shown in Figure 12.

The rates of convergence of FM implementations are very similar to the rate of convergence of DFM, i.e., they have a first order rate of convergence. The meshfree implementation using an irregular nodal distribution provided the lowest convergence rate of 0.93 and indicates that the nodal distribution does affect the rate of convergence of the meshfree numerical scheme. The comparative convergence rates obtained between DFM and FM implementations indicate that the fracture mapping approach solution accuracy is similar to that of DFM, specifically when considering the reduced number of nodes within the domain required to achieve the solution.
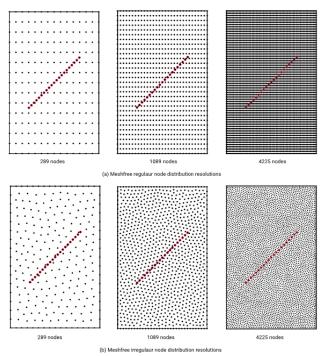

Figure 11. Domain discretizations used to determine the rates of convergence of the FEM and Meshfree fracture mapping implementation
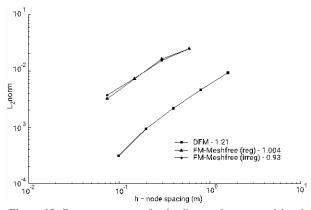

Figure 12. Convergence rates for the discrete fracture model and the meshfree fracture mapping approach

The pressure fields determined for the discrete fracture model and the proposed meshfree fracture mapping method were also compared. The discretizations used to determine the pressure fields are shown in Figure 13 and the resulting pressure fields are shown in Figure 14 Since differences in the pressure fields obtained for the different methods are indistinguishable, a pressure profile along a vertical section through the centre of the domain was created to compare the pressure change across the domain for each model.
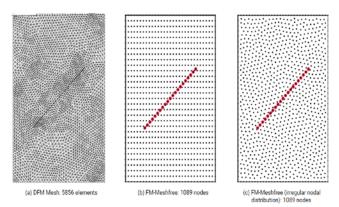
Figure 13. Domain discretizations used to determine pressure fields for comparison

Using the discrete fracture model as a baseline for comparison, the proposed meshfree fracture mapping method adequately describes the variation in pressure across the domain (see Figure 15). It should be noted that the meshfree fracture mapping discretizations used to generate the pressure fields are all at resolutions lower than that of DFM.
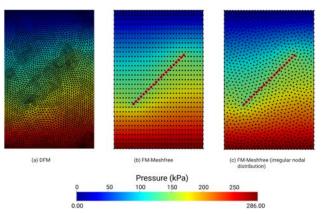

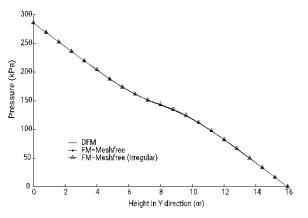**Figure 14.** Pressure fields obtained for DFM and meshfree fracture mapping implementation

Figure 15. Pressure profile for a vertical section taken through the centre of the fractured domain

10. Conclusion

The meshfree fracture mapping presented is able to adequately simulate the fluid flow in a fractured porous domain without the need for intensive mesh refinement required for discrete fracture models. The method also produces results that are in good agreement with analytical results presented in literature. Although direct nodal integration has been used for the meshfree implementation, the use of the Taylor series expansion terms eliminate instabilities in the solution obtained. Accuracy of the method can be improved by increasing the number of nodes used to discretize the fracture.

References:

Barenblatt, G.I., Zheltov, I.P., and Kochina, I.N. (1960), "Basic concepts in the theory of seepage of homogeneous liquids in fissured rocks [strata]", *Journal of Applied Mathematics and Mechanics*, Vol.24, pp.1286-1303.

Bear, J. (1988), *Dynamics of Fluids in Porous Media*, Dover, New York.

Beissel, S., and Belytschko, T. (1996), "Nodal integration of the element-free Galerkin method", *Computer Methods in Applied Mechanics and Engineering*, Vol.139, pp.49-74 DOI: Doi: 10.1016/s0045-7825(96)01079-1.

Belytschko, T., Lu, Y.Y., and Gu, L. (1994), "Element-free Galerkin methods", *International Journal for Numerical Methods in Engineering*, Vol.37, pp.229-256.

Breitkopf, P., Rassineux, A., Touzot, G., and Villon, P. (2000), "Explicit form and efficient computation of MLS shape functions and their derivatives", *International Journal for Numerical Methods in Engineering*, Vol.48, pp.451-466.

Chen, J.-S., Wu, C.-T., Yoon, S. and You, Y. (2001), "A stabilised conforming nodal integration for Galerkin mesh-free methods", *International Journal for Numerical Methods in Engineering*, Vol.50, pp.435-466.

Cundall, P.A. and Strack, O.D.L. (1979), "A discrete numerical model for granular assemblies", *Geotechnique*, Vol.29, pp.47-64.

Danielson, K.T., Hao, S., Liu, W.K., Aziz Uras, R. and Li, S. (2000), "Parallel computation of meshless methods for explicit dynamic analysis", *International Journal for Numerical Methods in Engineering*, Vol.47, pp.1323-1341.

Diodato, D.M. (1994), "A compendium of fracture flow models", Work sponsored by U.S. Department of Defense, United States Army, Europe, Combat Maneuver Training Center, Hohenfels, Germany (Nov 1994).

Fung, L.S.K. (1991), "Simulation of block-to-block processes in naturally fractured reservoirs", *SPE Reservoir Engineering*, Vol.6, pp.477-484 DOI: 10.2118/20019-pa.

Geiger-Boschung, S., Huangfu, Q., Reid, F., Matthai, S.K., Coumou, D., Belayneh, M., Fricke, C., and Schmid, K.S. (2009). "Massively parallel sector scale discrete fracture and matrix simulations", *SPE Reservoir Simulation Symposium*, The Woodlands, Texas, USA, SPE 118924-MS.: Society of Petroleum Engineers.

Golberg, M. (1996), "Recent developments in the numerical evaluation of particular solutions in the boundary element method", *Applied Mathematics and Computation*, Vol.75, pp.91-101 DOI: Doi: 10.1016/0096-3003(95)00123-9.

Gringarten, A.C., Henry, J., Ramey, J., and Raghavan, R. (1974), "Unsteady-state pressure distributions created by a well with a single infinite-conductivity vertical fracture", *Society of Petroleum Engineers Journal*, Vol.14, pp.347-360 DOI: 10.2118/4051-pa.

Istok, J.D. (1989), *Groundwater Modeling by the Finite Element Method*, Washington, DC, American Geophysical Union.

Karimi-Fard, M., Durlofsky, L.J., and Aziz, K. (2004), "An efficient discrete-fracture model applicable for general-purpose reservoir simulators", *Society of Petroleum Engineers Journal*, Vol.9, pp.227-236. SPE 88812-PA DOI: DOI: 10.2118/88812-pa.

Kim, J.G., and Deo, M.D. (2000), "Finite element, discrete-fracture model for multiphase flow in porous media", *AIChE Journal*, Vol.46, pp.1120-1130.

Lamb, A.R. (2011), *Coupled Deformation, Fluid Flow and Fracture Propagation in Porous Media*. Doctor of Philosophy (PhD), Imperial College, London.

Lancaster, P., and Salkauskas, K. (1981), "Surfaces generated by moving least squares methods", *Mathematics of Computation*, Vol.37, pp.141-158.

Lee, J., Choi, S.-U., and Cho, W. (1999), "A comparative study of dual-porosity model and discrete fracture network model", *KSCE Journal of Civil Engineering*, Vol.3, pp.171-180.

Liu, G.R. (2010), *Meshfree Methods: Moving beyond the Finite Element Method*, CRC Press, Boca Raton.

Liu, G. R., and Gu, Y.T. (2001), "A point interpolation method for two-dimensional solids", *International Journal for Numerical Methods in Engineering*, Vol.50, pp.937-951.

Liu, G.R., Zhang, G.Y., Wang, Y.Y., Zhong, Z.H., Li, G.Y., and Han, X. (2007), "A nodal integration technique for meshfree radial point interpolation method (NI-RPIM)", *International Journal of Solids and Structures*, Vol.44, pp.3840-3860 DOI: 10.1016/j.ijsolstr.2006.10.025.

Lu, Y.Y., Belytschko, T., and Gu, L. (1994), "A new implementation of the element-free Galerkin method", *Computational Methods in Applied Mechanics and Engineering*, Vol.113, pp.397-414.

Matthäi, S.K., Mezentsev, A.A., and Belayneh, M. (2007), "Finite element-node-centered finite-volume two-phase-flow experiments with fractured rock represented by unstructured hybrid-element meshes", *SPE Reservoir Evaluation and Engineering*, Vol.10, pp.740-756. SPE 93341-PA DOI: DOI: 10.2118/93341-pa.

Onate, E., Idelsohn, S., Zienkiewicz, O.C., and Taylor, R.L. (1996), "A finite point method in computational mechanic-applications to convective transport and fluid flow", International *Journal for Numerical Methods in Engineering*, Vol.39, pp.3839-3866.

Rycroft, C.H., Grest, G.S., Landry, J.W., and Bazant, M.Z. (2006), "Analysis of granular flow in a pebble-bed nuclear reactor", *Physical Review E*, Vol.74, pp.021306.

Tran, N.H., and Ravoof, A. (2007), "Coupled fluid flow through discrete fracture network: A novel approach", *International Journal of Mathematics and Computers in Simulation*, Vol.1, pp.295-299.

Wagner, G.J., and Liu, W.K. (2000), "Application of essential boundary conditions in mesh-free methods: A corrected collocation method", *International Journal for Numerical Methods in Engineering*, Vol.47, pp.1367-1379.

Wang, J.G., and Liu, G.R. (2002), "A point interpolation meshless method based on radial basis functions", *International Journal for Numerical Methods in Engineering*, Vol.54, pp.1623-1648.

Warren, J.E., and Root, P.J. (1963), "The behavior of naturally fractured reservoirs", *Society of Petroleum Engineers Journal*, Vol.3, pp.245-255. SPE 426-PA DOI: DOI: 10.2118/426-pa.

Witherspoon, P.A., Wang, J.S.Y., Iwai, K., and Gale, J.E. (1980), "Validity of cubic law for fluid flow in a deformable rock fracture", *Water Resources Research*, Vol.16, pp.1016-1024 DOI: 10.1029/WR016i006p01016.

Zhang, X., and Sanderson, D.J. (2002), *Numerical Modelling and Analysis of Fluid Flow and Deformation of Fractured Rock Masses*, Elsevier Science, Oxford.

Authors' Biographical Notes:

Anthony R. Lamb *is the Director of Engineering at AID (Analytically Informed Design) Consulting Limited based in Trinidad and Tobago. He received a BSc degree in Civil Engineering from The University of the West Indies, St. Augustine Campus, Trinidad and Tobago (2000) as well as an MSc degree in Computational Modelling and Finite Elements in Engineering Mechanics from the University of Wales Swansea (2004), UK and a PhD Degree in Earth Science and Engineering Research with a specialisation in Computational Geomechanics from Imperial College London (2011). Dr. Lamb is a Chartered Engineer (CEng) and a Fellow of the Institution of Civil Engineers (UK) – FICE and a Fellow of the Institute of Marine Engineering, Science and Technology (UK) – FIMarEST. Anthony is also a registered engineer with the Board of Engineering of Trinidad and Tobago and specialises in finite element analysis (FEA), computational fluid dynamics (CFD) and computational geomechanics.*

Deborah Villarroel-Lamb *is a Lecturer in the Department of Civil and Environmental Engineering at the University of the West Indies, St. Augustine. She received a BSc (2000) and PhD (2007) degree in Civil Engineering from the University of the West Indies, St. Augustine Campus, Trinidad and Tobago. Dr. Villarroel-Lamb is a past recipient of the Newton Internal Fellowship from the The Royal Society (UK), 2009-2011 and also a Fellow of the Royal Society of Arts (FRSA). Deborah specialises in coastal engineering, which includes ocean hydrodynamics, coastal morphology and coastal engineering solutions.*

■